

Unsupervised Single-shot Depth Estimation using Perceptual Reconstruction

Christoph Angermann¹, Matthias Schwab¹, Markus Haltmeier¹, Christian Laubichler³, and Steinbjörn Jónsson²

¹Department of Mathematics, University of Innsbruck, Technikerstraße 13, 6020 Innsbruck, Austria

applied-math.uibk.ac.at

³LEC GmbH, Inffeldgasse 19, 8010 Graz, Austria

www.lec.at

²INNIO Jenbacher GmbH & Co OG, Achenseestrasse 1-3, 6200 Jenbach, Austria

www.innio.com/en

February 1, 2022

Abstract

Real-time estimation of actual object depth is a module that is essential to performing various autonomous system tasks such as 3D reconstruction, scene understanding and condition assessment of machinery parts. During the last decade of machine learning, extensive deployment of deep learning methods to computer vision tasks has yielded approaches that succeed in achieving realistic depth synthesis out of a simple RGB modality. While most of these models are based on paired depth data or availability of video sequences and stereo images, methods for single-view depth synthesis in a fully unsupervised setting have hardly been explored. This study presents the most recent advances in the field of generative neural networks, leveraging them to perform fully unsupervised single-shot depth synthesis. Two generators for RGB-to-depth and depth-to-RGB transfer are implemented and simultaneously optimized using the Wasserstein-1 distance and a novel perceptual reconstruction term. To ensure that the proposed method is plausible, we comprehensively evaluate the models using industrial surface depth data as well as the Texas 3D Face Recognition Database and the SURREAL dataset that records body depth. The success observed in this study suggests the great potential for unsupervised single-shot depth estimation in real-world applications.

1 Introduction

Real-time depth inference of a given object is a highly important computer vision task which can be applied in various robotic tasks such as simultaneous localization and mapping [1, 2, 3] as well as autonomous quality inspection in industrial applications [4, 5]. As the popularity of VR applications has continued to grow, instant depth estimation has also become an integral part of modeling complex 3D information out of single 2D images of human faces [6, 7] or body parts [8, 9, 10]. Depth information about an object can be directly obtained from sensors for optical distance measurement. Time-of-Flight (ToF) cameras, LIDAR or stereo imaging systems are often used in practice and were also employed to generate paired RGB-depth data from some well-known depth databases [1, 2, 8, 10, 11, 12, 13]. Since these sensors are typically very expensive time-consuming devices that are also subject to external influences, their applicability to fast full-image depth generation on small on-site devices is limited. These limitations have motivated depth synthesis out of a much simpler modality in terms of acquisition effort, namely an RGB image. This development has initiated a completely new field of research in computer vision. An important contribution was made by [14], who proposed deep convolutional neural networks (DCNNs) for monocular depth synthesis of indoor and outdoor scenes.

Basically, monocular single-image depth estimation out of RGB images can be seen as a modality transfer in which observed data of a simpler modality is mapped to desired properties of a more complex modality. Although DCNNs are a promising approach that succeed on such transfer tasks, they are commonly based on large amounts of training data, and generation and acquisition can be a demanding task. In the supervised setting in particular, DCNNs make use of paired training data during network parameter optimization, i.e., the network is provided with a single-view RGB and corresponding per-pixel depth [6, 10, 14, 15]. Since large scale dense depth profiles are not abundant in many applications, supervised approaches are not feasible for these objects. One possible way to remedy these shortcomings of supervised methods is to consider self-supervised approaches based on monocular video clips in which a supervisory depth counterpart is extracted from pose changes between adjacent frames. These models can be trained on RGB sequences in a self-supervised manner, where a depth network and a pose estimation network are simultaneously optimized via sophisticated view-synthesis losses [3, 16, 17, 18]. Obviously, these methods require non-static scenes or a moving camera position (e.g., moving humans [18], autonomous driving [2]). Nevertheless, the availability of monocular sequences of a moving scene is not always guaranteed.

A very recent example of this issue is provided by surface depth estimation of cylinder liners in large internal combustion engines for stationary power generation [4, 5]. Cylinder condition can be assessed from a depth profile on a micrometer scale of the measured area (cf. Figure 1). Current standards have the disadvantage that microscopic depth sensing of cylinder liner surface areas is a time-consuming and resource-intensive task which consists of disassembling the liner, removing it from the engine, cutting it into segments and measuring them with a highly expensive and stationary confocal microscope [4]. With a handheld microscope, however, single RGB records of the liner's inner surface can be generated from which depth profiles are synthesized. Since depth data is generated on a quite small scale ($1.9 \times 1.9 \text{ mm}^2$) and is comparatively high resolved, it is hardly possible to generate RGB data with accurately aligned pixel positions. This drawback confirms how a fully unsupervised approach is required in order to guarantee reasonable depth synthesis of this static scene.

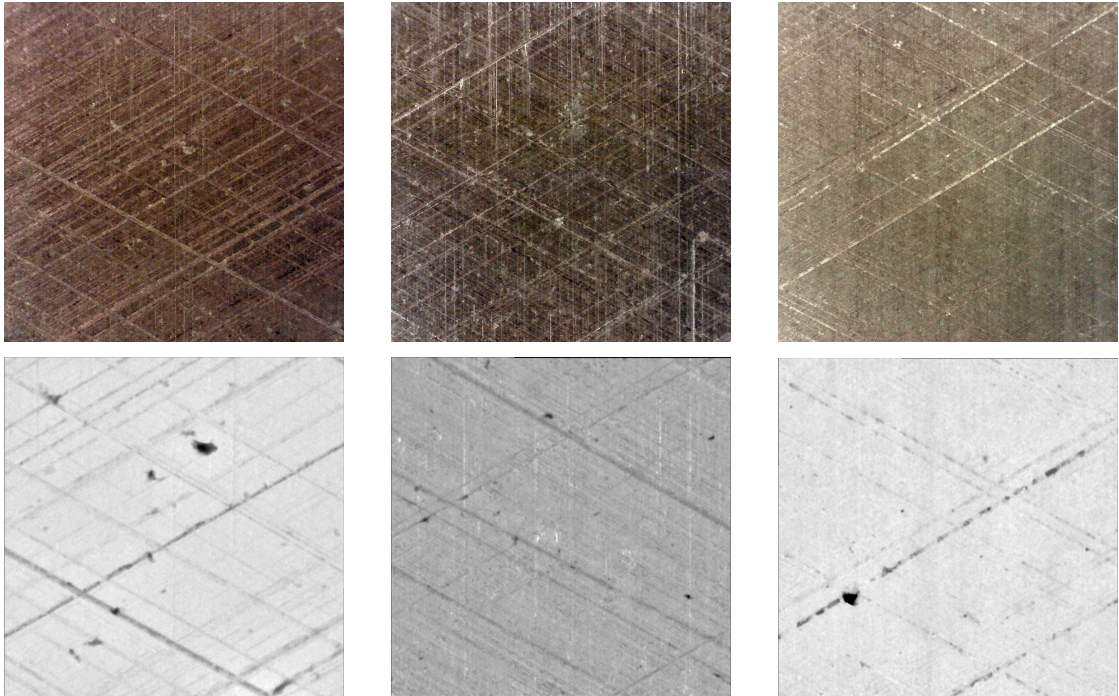


Figure 1: Top: RGB measurements of the inner surface of three cylinder liners with a spatial range of $4.2 \times 4.2 \text{ mm}^2$, recorded by a handheld microscope. Bottom: Depth profile of the same cylinder with a spatial range of $1.9 \times 1.9 \text{ mm}^2$, measured with a confocal microscope. The pixels of the modalities are not aligned.

Several recent advances in unpaired modality and style transfer are based on generative adversarial models (GAN) [19], cycle-consistency [20] and probabilistic distance measures [21, 22]. The method proposed in this paper leverages established model architectures and training strategies in deep learning to unpaired single-view depth

synthesis and is tested on the afore mentioned industrial application of surface depth estimation. Furthermore, the approach is applied to other datasets to create realistic scenarios when perfectly aligned RGB-depth data is not available in practice. More precisely, we test the model on the Texas 3D Face Recognition database (Texas-3DFRD) [12] and show its plausibility in an unsupervised setting when there is little available data. The SURREAL dataset [9] is used to test performance on RGB-D videos of human bodies, where RGB and depth frames are not perfectly aligned.

Contributions:

- This study finds a solution to the industrial modality transfer problem of single-shot surface depth estimation, which is then applied to the completely different tasks of unsupervised face depth and human body depth synthesis. This indicates the universality of the approach.
- To the best of our knowledge, this is the first research conducted on single-view depth estimation in a fully unsupervised setting and using GANs that are optimized via the Wasserstein-1 distance and a perceptual reconstruction loss. Therefore, this paper provides comprehensive results and experiments on an architecture that combines recent progress in unsupervised and adversarial learning and of which hardly any empirical observations exist.

2 Related Work

The following section summarizes the most important milestones in the development of generative adversarial networks and highlights recent works on depth synthesis via GANs. Appendix A presents some 3D databases that have been critical to the development of deep learning-based models for depth estimation.

2.1 Generative Adversarial Networks

A vanilla GAN [19] consists of a generator network $G : \mathcal{Z} \rightarrow \mathcal{X}$ mapping from a low-dimensional latent space \mathcal{Z} to image space \mathcal{X} , where parameters of the generator are adapted so that the distribution of generated examples assimilates the distribution of a given data set. To be able to assess any similarity between arbitrary high-dimensional image distributions, a discriminator $f : \mathcal{X} \rightarrow [0, 1]$ is trained simultaneously to distinguish between generator distribution and real data distribution. In a two-player min-max game, generator parameters are then updated to fool a steadily improving discriminator. Usage of the initially proposed discriminator approach can cause the vanishing gradient problem and does not provide any information on the real distance between the generator and the real distribution. This issue has been discussed thoroughly in [21], where the problem is bypassed by replacing the discriminator with a critic network that approximates the Wasserstein-1 distance [23] between the real distribution and the generator distribution.

While the quintessence of GANs is to draw synthetic instances following a given data distribution, cycle-consistent GANs [20] allow one-to-one mappings between two image domains \mathcal{X} and \mathcal{Y} . In essence, two generator networks $G_{\mathcal{Y}} : \mathcal{X} \rightarrow \mathcal{Y}, G_{\mathcal{X}} : \mathcal{Y} \rightarrow \mathcal{X}$ and corresponding discriminator networks $f_{\mathcal{Y}} : \mathcal{Y} \rightarrow [0, 1], f_{\mathcal{X}} : \mathcal{X} \rightarrow [0, 1]$ are trained simultaneously to enable generation of synthetic instances for both image domains (e.g., synthesizing a winter landscapes from summer scenes and vice versa). To ensure one-to-one correspondence, a cycle-consistency term is added to the two adversarial loss functionals. Although cycle-consistent GANs had initially been constructed for style transfer purposes, they were also very well received in the area of modality transfer in biomedical applications [24, 25, 26]. Since optimization and parameter fine-tuning of GANs often turns out to be extremely demanding and time-intensive, much research has emphasized stabilization of the training process through the development of stable network architectures such as DCGAN [27] or PatchGAN [28].

2.2 Depth Estimation using GAN

While style transfer emphasizes the modification of a given modality, modality transfer makes it possible to switch the domains even when they are defined in distinct dimensional spaces. Use of left-right consistency and a GAN architecture results in excellent unsupervised depth estimation based on stereo images [29, 30]. In [31] and [32], a GAN has been trained to perform unpaired depth synthesis out of single monocular images. To this end, GANs

were employed in the context of domain adaptation using an additional synthesized data set of the same application with paired samples. This approach may not be regarded as a fully unsupervised method and requires availability or construction of a synthetic dataset. [6] consider a conditional GAN (CGAN) [28] for solving single-image face depth synthesis. Nevertheless, CGANs rely on paired data since the adversarial part estimates the plausibility of an input-output pair. Another interesting approach was tried in [15], where indoor depth and segmentation were estimated simultaneously using cycle-consistent GANs. The cycle-consistency loss helped them to maintain the characteristics of the RGB input during depth synthesis while the simultaneous segmentation resolved the fading problem in which depth information is hidden by larger features. However, the proposed discriminator network and reconstruction term in the generator loss function are based on paired RGB and depth/segmentation data.

Since aligned data pairs, segmentation maps, monocular sequences or synthetic data samples are not available for the aforementioned industrial application of surface depth synthesis, this paper introduces the latest advances in GAN architectures and corresponding training techniques to the research field of fully unsupervised single-shot depth estimation.

3 Method

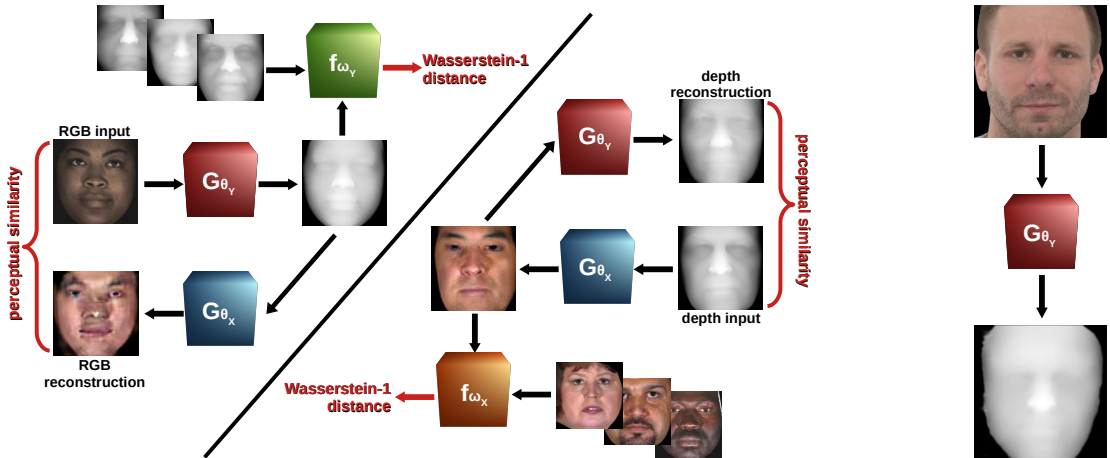


Figure 2: Illustration of the proposed framework: The left part describes the domains in which the RGB-to-depth generator G_{θ_y} and the contrary depth-to-RGB generator G_{θ_x} operate. Both generators are updated via the probabilistic Wasserstein-1 distance, estimated by f_{ω_y} in the input and f_{ω_x} in the target domain. Perceptual similarity is compared between each generator input and its reconstruction. The right plot indicates that during inference, only G_{θ_y} has to be deployed to synthesize new depth profiles. RGB images and ground truth depth images were taken from the Texas-3DFRD [12].

This section proposes an approach to monocular single-image depth synthesis with unpaired data and discusses the introduced framework and training strategy in detail.

3.1 Setting and GAN Architecture

The underlying structure of the proposed modality synthesis are two GANs linked with a reconstruction term (cf. Figure 2). To be more exact, let $\mathcal{X} \subset [0, 255]^{d_1 \times d_2 \times 3}$ and $\mathcal{Y} \subset \mathbb{R}^{d_1 \times d_2 \times 1}$ denote the domain of RGB and depth images, respectively, where the number of image pixels $d_1 \cdot d_2$ is the same in both domains. Furthermore, let $X := \{x_1, \dots, x_M\}$ be the set of M given RGB images and $Y := \{y_1, \dots, y_N\}$ the set of N available but unaligned depth profiles. P_X and P_Y denote the distributions of the images in both domains. The proposed model includes a generator function $G_{\theta_y} : \mathcal{X} \rightarrow \mathcal{Y}$, which aims to map an input RGB image to a corresponding depth counterpart in the target domain. A generator function for image transfer may be approximated by a DCNN, which is parameterized by a weight vector θ_y consisting of several convolution kernels. By adjusting θ_y , the

distribution of generator outputs P_{θ_y} may be brought closer to the real data distribution in the depth domain P_y . Note we do not know what P_{θ_y} and P_y actually look like, we only have access to unpaired training samples $G_{\theta_y}(x) \sim P_{\theta_y}$, $x \in X$ and $y \sim P_y$, $y \in Y$. An adversarial approach is deployed to ensure assimilation of both high-dimensional distributions in the GAN setting. The distance between the generator distribution and the real distribution is estimated by an additional DCNN $f_{\omega_y} : \mathcal{Y} \rightarrow \mathbb{R}$, which is parameterized by weight vector ω_y and is trained simultaneously with the generator network since P_{θ_y} changes after each update to the generator weights θ_y . This ensures that G_{θ_y} can be pitted against a steadily improving loss network f_{ω_y} [19].

This research work has chosen a network critic based on the Wasserstein-1 distance [21, 23]. The Wasserstein-1 distance (earth mover distance) between two distributions P_1 and P_2 is defined as $\mathcal{W}_1(P_1, P_2) := \inf_{J \in \mathcal{J}(P_1, P_2)} \mathbb{E}_{(x, y) \sim J} \|x - y\|$, where the infimum is taken over the set of all joint probability distributions that have marginal distributions P_1 and P_2 . Since the exact computation of the infimum is highly intractable, the Kantorovich-Rubinstein duality [23] is used:

$$\mathcal{W}_1(P_1, P_2) = \sup_{\|f\|_L \leq 1} \left[\mathbb{E}_{y \sim P_1} f(y) - \mathbb{E}_{y \sim P_2} f(y) \right], \quad (1)$$

where $\|\cdot\|_L \leq C$ denotes that a function is C -Lipschitz. Equation (1) indicates that a good approximation to $\mathcal{W}_1(P_y, P_{\theta_y})$ is found by maximizing the distance $\mathbb{E}_{y \sim P_y} f_{\omega_y}(y) - \mathbb{E}_{y \sim P_{\theta_y}} f_{\omega_y}(y)$ over the set of DCNN weights $\{\omega_y \mid f_{\omega_y} : \mathcal{Y} \rightarrow \mathbb{R} \text{ 1-Lipschitz}\}$, where the Lipschitz continuity of f_{ω_y} can be enhanced via a gradient penalty [22]. Given training batches $\mathbf{y} = \{y_n\}_{n=1}^b$, $y_n \stackrel{\text{iid}}{\sim} P_y$ and $\mathbf{x} = \{x_n\}_{n=1}^b$, $x_n \stackrel{\text{iid}}{\sim} P_x$, this yields the following empirical risk for critic f_{ω_y} :

$$\mathcal{R}_{\text{cri}}(\omega_y, \theta_y, p, \mathbf{y}, \mathbf{x}) := \frac{1}{b} \sum_{n=1}^b \left[f_{\omega_y}(G_{\theta_y}(x_n)) - f_{\omega_y}(y_n) + p \cdot \left(\left(\|\nabla_{\tilde{y}_n} f_{\omega_y}(\tilde{y}_n)\|_2 - 1 \right)_+^2 \right) \right], \quad (2)$$

where p denotes the influence of the gradient penalty, $(\cdot)_+ := \max(\{0, \cdot\})$ and $\tilde{y}_n := \epsilon_n \cdot G_{\theta_y}(x_n) + (1 - \epsilon_n) \cdot y_n$ for $\epsilon_n \stackrel{\text{iid}}{\sim} \mathcal{U}[0, 1]$. The goal of the RGB-to-depth generator G_{θ_y} is to minimize the distance. Since only the first term of the functional in (2) depends on the generator weights θ_y , the adversarial empirical risk for generator G_{θ_y} simplifies as follows:

$$\mathcal{R}_{\text{adv}}(\theta_y, \omega_y, \mathbf{x}) := -\frac{1}{b} \sum_{n=1}^b f_{\omega_y}(G_{\theta_y}(x_n)). \quad (3)$$

3.2 Perceptual Reconstruction

In the context of depth synthesis, it is not sufficient to ensure that the output samples lie in the depth domain. Care must be taken that synthetic depth profiles do not become irrelevant to the input. A reconstruction constraint forces generator input and output to share same spatial structure by taking into account the similarity between the input and the reconstruction of the synthesized depth profile. Obviously, calculation of a reconstruction error requires an opposite generator function $G_{\theta_x} : \mathcal{Y} \rightarrow \mathcal{X}$ to assimilate real RGB distribution P_x as well as the corresponding distance network $f_{\omega_x} : \mathcal{X} \rightarrow \mathbb{R}$. Both have to be optimized simultaneously to the RGB-to-depth direction. The reconstruction error is commonly evaluated by assessing similarity between x and $G_{\theta_x}(G_{\theta_y}(x))$ as well as similarity between y and $G_{\theta_y}(G_{\theta_x}(y))$ for $x \in \mathcal{X}$ and $y \in \mathcal{Y}$. In the setting of style transfer and cycle-consistent GANs [20], a pixelwise distance function on image space is considered, where the mean absolute error (MAE) or the mean squared error (MSE) are common choices.

The use of a contrary generator G_{θ_x} can be viewed as a type of regularization since it prevents mode collapse, i.e., generator outputs remain dependent on the inputs. Deployment of the cycle-consistency approach [20], where reconstruction error is measured in image space, assumes no information loss during the modality transition. This corresponds to the applications of summer-to-winter landscape or photograph-to-Monet painting transition. Determining G_{θ_y} and G_{θ_x} is an ill-posed problem since a single depth profile may be generated by an infinite number of distinct RGB images and vice versa [33]. For example, during RGB-to-depth transition of human faces, information on image brightness, light source or the subject's skin color is lost. As a consequence, the contrary depth-to-RGB generator needed for regularization has to synthesize the lost properties of the image. Both generators

G_{θ_y} and G_{θ_x} may be penalized if the skin color or the brightness of the reconstruction is changed even though G_{θ_x} did exactly what we expected it to do, i.e., synthesize a human face that is related to the input's depth profile. Adapting the idea of [34], we propose a perceptual reconstruction loss, i.e., instead of computing a reconstruction error in image space, we consider certain image features of the reconstruction. Typical perceptual similarity metrics extract features by propagating the images (to be compared) through an auxiliary network that is usually pretrained on a large image classification task [34, 35, 36]. Nevertheless, we expect our feature extractor to be perfectly tailored to our data and not determined by an additional network pretrained on a very general classification task [35] that may not even cover our type of data. Therefore, we enforce the reconstruction consistency on the image space by using the MAE loss on feature vectors extracted by $\phi_x(\cdot) := f_{\omega_x}^l(\cdot)$, which corresponds to the l -th layer of the RGB critic (cf. Algorithm 1). Analogously, we define the feature extractor on depth space by $\phi_y(\cdot) := f_{\omega_y}^l(\cdot)$, which corresponds to the l -th layer of the depth critic. Although we are aware that feature extractor weights are adjusted with each update of critic weights ω_x, ω_y , we assume that, at least at a later stage of training, ϕ_x and ϕ_y have learned good and stable features on the image and depth domain. This yields the following empirical reconstruction risk:

$$\begin{aligned} \mathcal{R}_{\text{rec}}(\theta_x, \theta_y, \phi_x, \phi_y, \mathbf{x}, \mathbf{y}) := & \frac{1}{b} \sum_{n=1}^b \text{MAE}[\phi_x(G_{\theta_x}(G_{\theta_y}(x_n))), \phi_x(x_n)] \\ & + \frac{1}{b} \sum_{n=1}^b \text{MAE}[\phi_y(G_{\theta_y}(G_{\theta_x}(y_n))), \phi_y(y_n)]. \end{aligned} \quad (4)$$

In our implementation, we set $l := L - 2$ for a critic with L layers, i.e., we use the second-to-last layer of the critic.

A good reconstruction term must still be found for the start of training when the critic features are not yet sufficiently reliable. At first, it is desirable to guide the framework to preserve structural similarity during RGB-to-depth and depth-to-RGB transition. Therefore, we propose to compare the input and its reconstruction in the image space while automatically removing the brightness, illumination and color of the RGB images beforehand. This can be ensured by applying the following steps:

1. Convert the image to grayscale by applying the function $g : [0, 255]^{d_1 \times d_2 \times 3} \rightarrow \mathbb{R}^{d_1 \times d_2}$, $x \mapsto \frac{0.299}{255} \cdot x_{(.,0)} + \frac{0.587}{255} \cdot x_{(.,1)} + \frac{0.144}{255} \cdot x_{(.,2)}$, where $(., i)$ denotes the i -th color channel for $i = 0, 1, 2$.
2. Enhance the brightness of the grayscale image using an automated gamma correction based on the image brightness [37], i.e. take the grayscale image x_{gr} to the power of $\Gamma(x_{\text{gr}}) := -0.3 \cdot 2.303 / \ln \bar{x}_{\text{gr}}$, where \bar{x}_{gr} denotes the average of the gray values.
3. Convolve the enhanced image with a high-pass filter h in order to dim the lighting source and color information (cf. Figure 3). The high-pass filter may be applied in Fourier domain, i.e., the 2D Fourier transform is multiplied by a Gaussian high-pass filter matrix H^σ defined by $H_{i,j}^\sigma := 1 - \exp\left(\left\|\left(i, j\right) - \left(\frac{d_1}{2}, \frac{d_2}{2}\right)\right\|_2^2 / (2\sigma^2)\right)$ for $i = 1, \dots, d_1$ and $j = 1, \dots, d_2$. In our implementation, $\sigma = 4$ yielded satisfactory results for all tasks.

This yields the updated empirical reconstruction risk:

$$\begin{aligned} \mathcal{R}_{\text{rec}}(\theta_x, \theta_y, \phi_x, \phi_y, \gamma, \mathbf{x}, \mathbf{y}) := & \gamma \cdot \frac{1}{b} \sum_{n=1}^b \text{MAE}[\phi_x(G_{\theta_x}(G_{\theta_y}(x_n))), \phi_x(x_n)] \\ & + \gamma \cdot \frac{1}{b} \sum_{n=1}^b \text{MAE}[\phi_y(G_{\theta_y}(G_{\theta_x}(y_n))), \phi_y(y_n)] \\ & + (1 - \gamma) \cdot \frac{1}{b} \sum_{n=1}^b \text{MAE}[\psi(G_{\theta_y}(G_{\theta_x}(x_n))), \psi(x_n)] \\ & + (1 - \gamma) \cdot \frac{1}{b} \sum_{n=1}^b \text{MAE}[G_{\theta_y}(G_{\theta_x}(y_n)), y_n], \end{aligned} \quad (5)$$

where $\psi(\cdot) := h * g(\cdot)^{\Gamma(g(\cdot))}$ and γ is gradually increased from 0 to 1 during training to control feature extractor reliability. In the far right column in Figure 3, we may observe the strong effect of operator ψ . For the face sample,

the face shape and the positions of the nose and the eyes are very clear, at the same time the low image brightness and the exposure direction are resolved. The main edges of the cylinder liner surfaces are clearly identifiable whereas the different brown levels and illumination inconsistencies of the input are no longer visible.

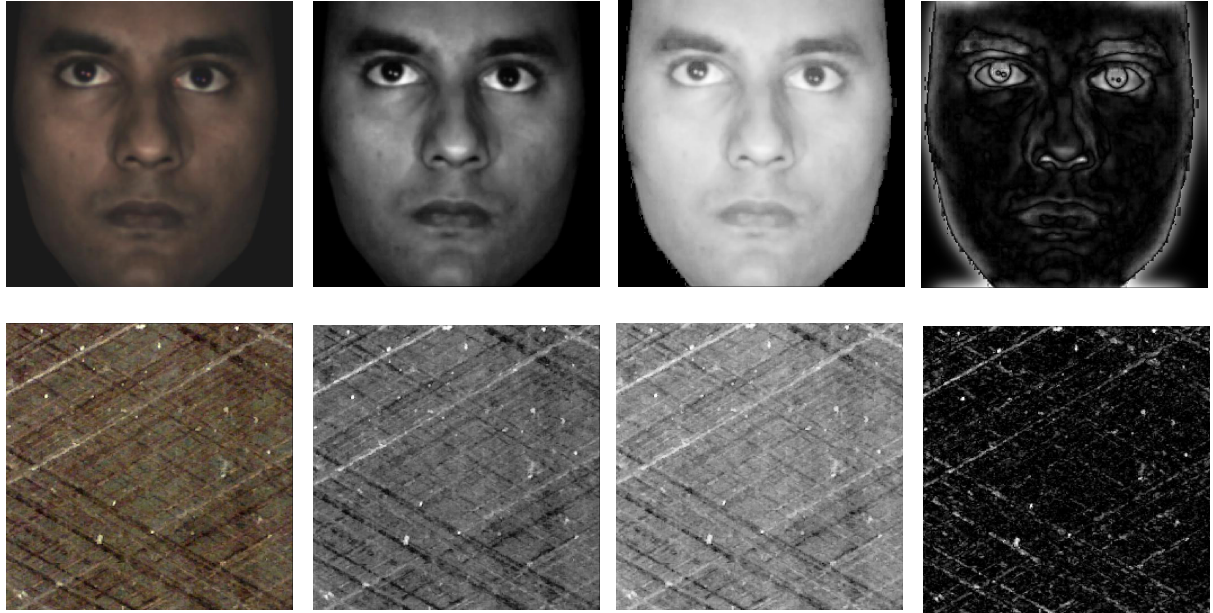


Figure 3: The first column visualizes the RGB samples and the second column the grayscale versions. The third column contains the gamma corrected counterparts, where the contrast in lower gray levels is enhanced for dark images in particular. The last column illustrates the application of the high-pass filter.

Using the previously discussed risk functions \mathcal{R}_{cri} (2), \mathcal{R}_{adv} (3) and \mathcal{R}_{rec} (5), Algorithm 1 summarizes the proposed architecture for fully unsupervised single-view depth estimation. Implementation of the proposed framework is publicly available on <https://github.com/anger-man/unsupervised-depth-estimation>.

3.3 Network Architectures

As critical as the loss function design of an unsupervised method is the choice of an appropriate architecture for the critic and the generator network. A decoder for the critic is built following the DCGAN constraints in [27] with approximately 15.3×10^6 parameters. For comparison, we also test our implementation using a PatchGAN critic of the same size that was initially proposed in [28]. Both architectures are empirically proven to perform quite stably over a variety of different generative tasks. Three differing approaches to the generator network were implemented in this study. The first generator is a ResNet18 [38] with a depth-specific upsampling part taken from [17] (19.8×10^6 parameters). The second architecture is a U-net [20] with 21.2×10^6 parameters, which was initially proposed in [39] and is often considered in biomedical applications [40, 41]. Lastly, we implemented an encoder-decoder network with several consecutive residual blocks as used by [20] for style transfer (11.4×10^6 parameters). Appendix B provides detailed information on all critic and generator implementations.

4 Experiments and Discussion

The framework proposed in Algorithm 1 is implemented with the publicly available TensorFlow framework [42]. The applications are inner surface depth estimation of cylinder liners, face depth estimation based on the Texas-3DFRD [12] and body depth synthesis using the SURREAL dataset [9]. This section briefly describes each dataset and separately presents and discusses its results. In our implementation, we set the number of generator updates n_G to 10k, the minibatch size b to 8 and the penalty term p to 100. The number of critic iterations n_f is initially established to be 24 to ensure a good approximation of the Wasserstein-1 distance in the beginning. After 1000

Algorithm 1 Proposed Framework

Require: α_f critic learning rate; α_G generator learning rate; p gradient penalty; n_f number of critic iterations; n_G number of generator updates; b minibatch size; λ_{rec} reconstruction loss weight

Require: ω_y, ω_x initial critic weights; θ_y, θ_x initial generator weights; $\gamma = 0$

for $k = 1, \dots, n_G$ **do**

for $i = 1, \dots, n_f$ **do**

 Sample $\mathbf{x} = \{x_n\}_{n=1}^b \subset X$ and $\mathbf{y} = \{y_n\}_{n=1}^b \subset Y$

$\{\tilde{y}_n\}_{n=1}^b \leftarrow \{\epsilon_n \cdot G_{\theta_y}(x_n) + (1 - \epsilon_n) \cdot y_n, \epsilon_n \sim \mathcal{U}[0, 1]\}_{n=1}^b$

$\{\tilde{x}_n\}_{n=1}^b \leftarrow \{\epsilon_n \cdot G_{\theta_x}(y_n) + (1 - \epsilon_n) \cdot x_n, \epsilon_n \sim \mathcal{U}[0, 1]\}_{n=1}^b$

$\partial_y \leftarrow \nabla_{\omega_y} \mathcal{R}_{\text{cri}}(\omega_y, \theta_y, p, \mathbf{y}, \mathbf{x})$

$\partial_x \leftarrow \nabla_{\omega_x} \mathcal{R}_{\text{cri}}(\omega_x, \theta_x, p, \mathbf{x}, \mathbf{y})$

$\omega_y \leftarrow \text{Adam}(\omega_y, \partial_y, \alpha_f, \beta_1 = 0, \beta_2 = 0.9)$

$\omega_x \leftarrow \text{Adam}(\omega_x, \partial_x, \alpha_f, \beta_1 = 0, \beta_2 = 0.9)$

end for

 Sample $\mathbf{x} = \{x_n\}_{n=1}^b \subset X$ and $\mathbf{y} = \{y_n\}_{n=1}^b \subset Y$; set ϕ_y, ϕ_x to l -th layer of $f_{\omega_y}, f_{\omega_x}$

$\partial_y \leftarrow \nabla_{\theta_y} \mathcal{R}_{\text{adv}}(\theta_y, \omega_y, \mathbf{x}) +$

$\lambda_{\text{rec}} \cdot \nabla_{\theta_y} \mathcal{R}_{\text{rec}}(\theta_x, \theta_y, \phi_x, \phi_y, \gamma, \mathbf{x}, \mathbf{y})$

$\partial_x \leftarrow \nabla_{\theta_x} \mathcal{R}_{\text{adv}}(\theta_x, \omega_x, \mathbf{y}) +$

$\lambda_{\text{rec}} \cdot \nabla_{\theta_x} \mathcal{R}_{\text{rec}}(\theta_x, \theta_y, \phi_x, \phi_y, \gamma, \mathbf{x}, \mathbf{y})$

$\theta_y \leftarrow \text{Adam}(\theta_y, \partial_y, \alpha_G, \beta_1 = 0, \beta_2 = 0.9)$

$\theta_x \leftarrow \text{Adam}(\theta_x, \partial_x, \alpha_G, \beta_1 = 0, \beta_2 = 0.9)$

$\gamma \leftarrow \frac{k}{n_G}$

end for

generator updates, it is halved to speed up training. Results are presented for selected critic (DG \triangleq DCGAN, PG \triangleq PatchGAN) and generator (R \triangleq ResNet18, U \triangleq U-net, S \triangleq style transfer) combinations. In the following section, a critic-generator combination is always tested on different values of $\alpha_f, \alpha_G, \lambda_{\text{rec}}$ and only the best run in terms of evaluation metrics is reported. To illustrate the superiority of our novel approach, we also report the best run of each task over all critic-generator combinations trained with the common used cycle-consistency approach [20] instead of the perceptual reconstruction term in (5).

4.1 Surface Depth

This study uses the same database initially proposed in [4] for depth estimation of inner cylinder liner surfaces of large internal combustion engines. Depth measurements cover a spatial region of $1.9 \times 1.9 \text{ mm}^2$, have a dimension of approximately 4000×4000 pixels and are acquired using a resource-intensive logistic chain as discussed in the introduction. The profiles denote relative depth with respect to the core area of the surface on a μm scale. The RGB data is taken from the same cylinder surfaces with a simple handheld microscope. The RGB measurements cover a region of $4.2 \times 4.2 \text{ mm}^2$ and have a resolution of nearly 1024×1024 pixels. Measurement positions are not perfectly aligned with the depth data. 592 random samples are obtained from each image domain. The RGB and depth data is then augmented separately to nearly 7000 samples via random cropping, flipping and gamma correction [37]. To make computation feasible with an *NVIDIA GeForce RTX 2080* GPU, each sample is resized to a dimension of 256×256 pixels. In order to assess the visual quality between two completely unaligned domains, we also generated depth profiles of 211 additional surface areas and registered them with great effort using shear transformations and a mutual information criterion. These evaluation samples are not included in the training database. During optimization, RGB images and depth profiles are scaled from $[0, 255]$ to $[-1, 1]$ and from $[-7.4, 1.8]$ to $[-1, 1]$, respectively, whereas evaluation metrics - the root mean squared error (RMSE) and the MAE - are calculated on the original depth scale. Table 1 presents the results of different critic-generator combinations (**Cri** \triangleq critic, **Gen** \triangleq generator, **PeRec** \triangleq if novel perceptual reconstruction loss is used).

With regard to regularization of the reconstruction with a standard cycle-consistency approach [20], the best results have been achieved using a ResNet18 generator and a PatchGAN critic (RMSE of $0.79 \mu\text{m}$ and MAE of $0.6 \mu\text{m}$). The same generator-critic combination together with our novel perceptual reconstruction functional in (5) significantly

Table 1: Unsup. surface depth estimation: The reported metrics are RMSE and MAE of the ground truth and the synthesized depth (RMSE|MAE) and are evaluated on unseen data (smaller is better).

Cri	Gen	PeRec	α_f	α_G	λ_{rec}	Metrics
DG	R	✓	1×10^{-4}	1×10^{-4}	100	0.736 0.57
DG	U	✓	2×10^{-4}	2×10^{-4}	160	0.747 0.58
DG	S	✓	1×10^{-4}	2×10^{-4}	100	0.825 0.60
PG	R	✓	5×10^{-5}	9×10^{-5}	50	0.707 0.56
PG	R	✗	1×10^{-4}	1×10^{-4}	20	0.790 0.60

outperforms the standard approach and achieves an RMSE of $0.707 \mu\text{m}$ and an MAE of $0.56 \mu\text{m}$. The worst yet still satisfactory results have been achieved using a style transfer generator linked with a DCGAN critic.

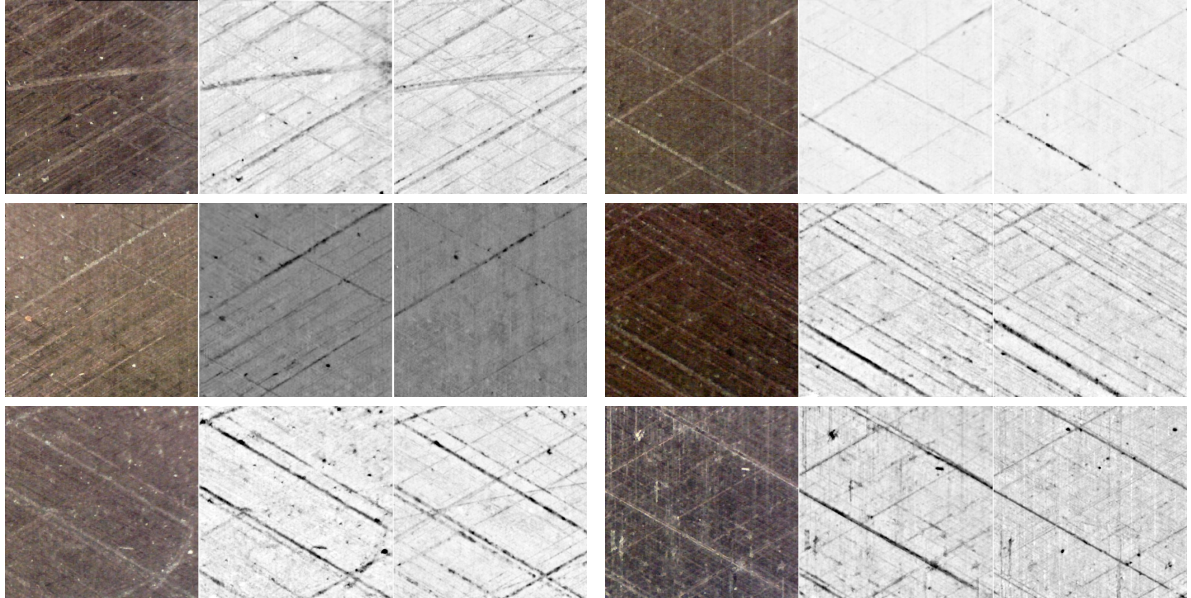


Figure 4: From left to right: Surface RGB input, synthesized surface depth (generated with ResNet18) and registered ground truth profile.



Figure 5: An instant 3D model generated by our proposed framework provides valuable information on liner surface condition.

4.2 Face Depth

The Texas-3DFRD [12] consists of 118 individuals and a variety of facial expressions and corresponding depth profiles are available for each of them. Depth pixels represent absolute depth and their values are in $[0, 1]$ where 1 represents the near clipping plane while 0 denotes the background. We randomly select 16 individuals as evaluation data and use the remaining samples as training data. For unsupervised training, we randomly select 50 % of the training individuals for the input domain and use the depth images of the remaining 50 % for the target domain. We resize all RGB frames and depth profiles to a dimension of 256×256 pixels. Data is augmented via flipping, histogram equalization and Gaussian blur to nearly 6300 samples per modality. During optimization, RGB images are scaled from $[0, 255]$ to $[-1, 1]$ and depth profiles are scaled from $[0, 1]$ to $[-1, 1]$, whereas the evaluation metrics RMSE and MAE are computed on the original depth scale. This application has been evaluated in a manner similar to the procedure in Section 4.1 and the results of different critic-generator combinations are presented in Table 2.

Table 2: Unsup. face depth estimation: The reported metrics are RMSE and MAE of the ground truth and the synthesized depth (RMSE|MAE) and are evaluated on unseen data (smaller is better).

Cri	Gen	PeRec	α_f	α_G	λ_{rec}	Metrics
DG	R	✓	5×10^{-5}	1×10^{-4}	80	0.071 0.05
DG	U	✓	5×10^{-5}	5×10^{-5}	160	0.083 0.06
DG	S	✓	5×10^{-5}	8×10^{-5}	100	0.080 0.05
PG	R	✓	5×10^{-5}	9×10^{-5}	2	0.074 0.05
PG	R	✗	5×10^{-5}	8×10^{-5}	2	0.082 0.06

The best results with standard cycle-consistency were achieved using a PatchGAN critic and a ResNet18 generator (RMSE of 0.082 and MAE of 0.06). The same generator in combination with a DCGAN critic and perceptual reconstruction significantly improved the results, yielding an RMSE of 0.071 and an MAE of 0.05. Obviously, ResNet18 clearly outperforms the other two generator architectures. More experiments on unsupervised and semi-supervised facial depth estimation with our method are presented in Appendix C.

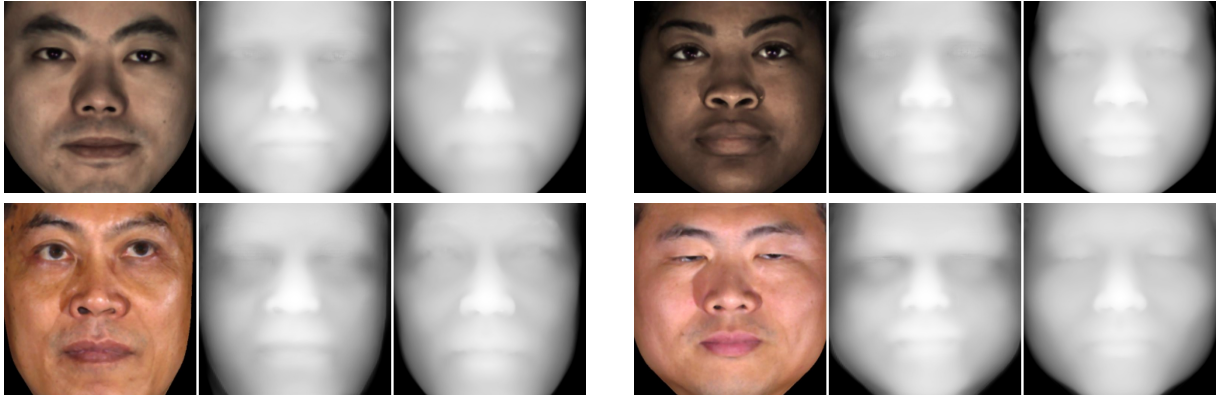


Figure 6: From left to right: Face RGB input, synthesized facial depth profile (generated with ResNet18) and corresponding ground truth profile.

4.3 Body Depth

The SURREAL dataset [9] consists of nearly 68k video clips that show 145 different synthetic subjects performing various actions. The clips consist of 100 RGB frames with perfectly aligned depth profiles that denote real-world camera distance. We use the same train/test split as [9], i.e., we remove nearly 12.5k clips and use the middle frame of each 100-frame clip for evaluation. For the remaining clips, an amount of 2500 clips is randomly selected for training. We choose 20 RGB and 20 depth frames per clip ensuring that RGB and depth frames are disjointed in order to mimic an application without any accurately aligned RGB-depth pairs. This results in approximately



Figure 7: An example of viewpoint augmentation using a 3D face model instantly generated by our proposed framework.

50k samples per modality. We strictly follow the preprocessing pipeline of [9], cropping each frame to the human bounding box and resizing/padding images to a dimension of 256×256 pixels. In addition, for each image, we subtract the median of depth values to fit the depth images into the range ± 0.4725 meters, where values less or equal -0.4725 denote background. During optimization, RGB images are scaled from $[0, 255]$ to $[-1, 1]$ and depth profiles are scaled from $[-0.4725, 0.4725]$ to $[-1, 1]$, whereas evaluation metrics RMSE and MAE are computed on the original depth scale. This application has been evaluated in a manner similar to the procedure in Section 4.1 and in Section 4.2 and the results of different critic-generator combinations are presented in Table 3.

Table 3: Unsup. body depth estimation: The reported metrics are RMSE and MAE of the ground truth and the synthesized depth (RMSE|MAE) and are evaluated on unseen data (smaller is better).

Cri	Gen	PeRec	α_f	α_G	λ_{rec}	Metrics
DG	R	✓	5×10^{-5}	2×10^{-4}	20	0.091 0.028
DG	U	✓	7×10^{-5}	2×10^{-4}	10	0.080 0.022
DG	S	✓	5×10^{-5}	2×10^{-4}	20	0.092 0.027
PG	U	✓	8×10^{-5}	2×10^{-4}	5	0.105 0.038
DG	U	✗	5×10^{-5}	8×10^{-5}	20	0.094 0.028

The best results with standard cycle-consistency were achieved using a DCGAN critic and a U-net generator (RMSE of 94 mm and MAE of 28 mm). Same critic-generator combination clearly improved the results when using perceptual reconstruction (RMSE of 80 mm and MAE of 22 mm). For comparison, [9] trained a body depth prediction model on all 55k training clips in a supervised manner and achieved an RMSE of 72.9 mm on the same test set.



Figure 8: From left to right: Body RGB input, synthesized depth profile (generated with U-net) and corresponding ground truth profile.

5 Conclusion

This paper proposes a framework for fully unsupervised single-shot depth estimation from monocular RGB images based on the Wasserstein-1 distance and a novel perceptual reconstruction loss. The model is comprehensively evaluated on differing depth synthesis tasks without using pairwise RGB and depth data during training. The approach provides a reasonable solution for estimating the relative depth of cylinder liner surfaces when generation of paired data is technically not feasible. Moreover, the proposed algorithm also shows promising results when applied to the task of absolute depth estimation of human bodies and faces, thereby proving that it may be generalized to other real-life tasks. However, one disadvantage of the perceptual reconstruction approach is that four neural networks must be fitted in parallel. Future work will therefore include the development of one-sided depth synthesis models in an unsupervised manner as well as the application of our approach to other modality transfer tasks.

Acknowledgements

The authors would like to acknowledge the financial support of the "COMET - Competence Centres for Excellent Technologies" Programme of the Austrian Federal Ministry for Climate Action, Environment, Energy, Mobility, Innovation and Technology (BMK) and the Federal Ministry for Digital and Economic Affairs (BMDW) and the Provinces of Styria, Tyrol and Vienna for the COMET Centre (K1) LEC EvoLET. The COMET Programme is managed by the Austrian Research Promotion Agency (FFG) [grant number 865843]

References

- [1] P. K. Nathan Silberman, Derek Hoiem and R. Fergus, "Indoor segmentation and support inference from rgbd images," in *ECCV*, 2012.
- [2] A. Geiger, P. Lenz, and R. Urtasun, "Are we ready for autonomous driving the KITTI vision benchmark suite," in *Conference on computer vision and pattern recognition (CVPR)*, 2012.
- [3] C. Zhao, Q. Sun, C. Zhang, Y. Tang, and F. Qian, "Monocular depth estimation based on deep learning: an overview," *Science china technological sciences*, pp. 1–16, 2020.
- [4] C. Angermann, S. Jónsson, M. Haltmeier, A. Moravová, C. Laubichler, C. Kiesling, M. Kober, and W. Fimml, "Machine learning for nondestructive wear assessment in large internal combustion engines," 2021.
- [5] C. Laubichler, C. Kiesling, M. Kober, A. Wimmer, C. Angermann, M. Haltmeier, and S. Jónsson, "Quantitative cylinder liner wear assessment in large internal combustion engines using handheld optical measurement devices and deep learning," in *18. Tagung Nachhaltigkeit in Mobilität, Transport und Energieerzeugung* (H. Eichlseder, ed.), IVT Mitteilungen/Reports, pp. 217–231, Verlag der Technischen Universität Graz, Sept. 2021.
- [6] A. T. Arslan and E. Seke, "Face depth estimation with conditional generative adversarial networks," *IEEE Access*, vol. 7, pp. 23222–23231, 2019.
- [7] F. Khan, S. Basak, H. Javidnia, M. Schukat, and P. Corcoran, "High-accuracy facial depth models derived from 3D synthetic data," in *2020 31st Irish signals and systems conference (ISSC)*, pp. 1–5, IEEE, 2020.
- [8] D. Vlasic, I. Baran, W. Matusik, and J. Popović, "Articulated mesh animation from multi-view silhouettes," in *ACM SIGGRAPH 2008 papers*, pp. 1–9, 2008.
- [9] G. Varol, J. Romero, X. Martin, N. Mahmood, M. J. Black, I. Laptev, and C. Schmid, "Learning from synthetic humans," in *Proceedings of the IEEE conference on computer vision and pattern recognition*, pp. 109–117, 2017.
- [10] S. Tang, F. Tan, K. Cheng, Z. Li, S. Zhu, and P. Tan, "A neural network for detailed human depth estimation from a single image," in *Proceedings of the IEEE/CVF international conference on computer vision*, pp. 7750–7759, 2019.

- [11] A. Savran, N. Alyüz, H. Dibeklioğlu, O. Çeliktutan, B. Gökberk, B. Sankur, and L. Akarun, “Bosphorus database for 3D face analysis,” in *European workshop on biometrics and identity management*, pp. 47–56, Springer, 2008.
- [12] S. Gupta, K. R. Castleman, M. K. Markey, and A. C. Bovik, “Texas 3D face recognition database,” in *2010 IEEE southwest symposium on image analysis & interpretation (SSIAI)*, pp. 97–100, IEEE, 2010.
- [13] C. Ionescu, D. Papava, V. Olaru, and C. Sminchisescu, “Human3.6m: large scale datasets and predictive methods for 3D human sensing in natural environments,” *IEEE transactions on pattern analysis and machine intelligence*, vol. 36, pp. 1325–1339, jul 2014.
- [14] D. Eigen, C. Puhrsch, and R. Fergus, “Depth map prediction from a single image using a multi-scale deep network,” *Advances in neural information processing systems*, vol. 27, pp. 2366–2374, 2014.
- [15] D.-h. Kwak and S.-h. Lee, “A novel method for estimating monocular depth using cycle gan and segmentation,” *Sensors*, vol. 20, no. 9, p. 2567, 2020.
- [16] T. Zhou, M. Brown, N. Snavely, and D. G. Lowe, “Unsupervised learning of depth and ego-motion from video,” in *Proceedings of the IEEE conference on computer vision and pattern recognition*, pp. 1851–1858, 2017.
- [17] C. Godard, O. Mac Aodha, M. Firman, and G. J. Brostow, “Digging into self-supervised monocular depth estimation,” in *Proceedings of the IEEE/CVF international conference on computer vision*, pp. 3828–3838, 2019.
- [18] Y. Jafarian and H. S. Park, “Learning high fidelity depths of dressed humans by watching social media dance videos,” in *Proceedings of the IEEE/CVF conference on computer vision and pattern recognition*, pp. 12753–12762, 2021.
- [19] I. Goodfellow, J. Pouget-Abadie, M. Mirza, B. Xu, D. Warde-Farley, S. Ozair, A. Courville, and Y. Bengio, “Generative adversarial nets,” in *Advances in neural information processing systems* (Z. Ghahramani, M. Welling, C. Cortes, N. Lawrence, and K. Q. Weinberger, eds.), vol. 27, Curran Associates, Inc., 2014.
- [20] J. Zhu, T. Park, P. Isola, and A. A. Efros, “Unpaired image-to-image translation using cycle-consistent adversarial networks,” in *2017 IEEE international conference on computer vision (ICCV)*, pp. 2242–2251, 2017.
- [21] M. Arjovsky, S. Chintala, and L. Bottou, “Wasserstein generative adversarial networks,” in *Proceedings of the 34th international conference on machine learning*, vol. 70, pp. 214–223, PMLR, 2017.
- [22] I. Gulrajani, F. Ahmed, M. Arjovsky, V. Dumoulin, and A. C. Courville, “Improved training of wasserstein GANs,” in *Advances in neural information processing systems* (I. Guyon, U. V. Luxburg, S. Bengio, H. Wallach, R. Fergus, S. Vishwanathan, and R. Garnett, eds.), vol. 30, Curran Associates, Inc., 2017.
- [23] C. Villani, *Optimal transport: old and new*, vol. 338. Springer science & business media, 2008.
- [24] X. Han, “MR-based synthetic CT generation using a deep convolutional neural network method,” *Medical physics*, vol. 44, no. 4, pp. 1408–1419, 2017.
- [25] Y. Hiasa, Y. Otake, M. Takao, T. Matsuoka, K. Takashima, A. Carass, J. L. Prince, N. Sugano, and Y. Sato, “Cross-modality image synthesis from unpaired data using cyclegan,” in *International workshop on simulation and synthesis in medical imaging*, pp. 31–41, Springer, 2018.
- [26] Y. Lei, J. Harms, T. Wang, Y. Liu, H.-K. Shu, A. B. Jani, W. J. Curran, H. Mao, T. Liu, and X. Yang, “MRI-only based synthetic CT generation using dense cycle consistent generative adversarial networks,” *Medical physics*, vol. 46, no. 8, pp. 3565–3581, 2019.
- [27] A. Radford, L. Metz, and S. Chintala, “Unsupervised representation learning with deep convolutional generative adversarial networks,” 2015.

[28] P. Isola, J.-Y. Zhu, T. Zhou, and A. A. Efros, “Image-to-image translation with conditional adversarial networks,” in *Proceedings of the IEEE conference on computer vision and pattern recognition*, pp. 1125–1134, 2017.

[29] A. Pilzer, D. Xu, M. Puscas, E. Ricci, and N. Sebe, “Unsupervised adversarial depth estimation using cycled generative networks,” in *2018 international conference on 3D vision (3DV)*, pp. 587–595, IEEE, 2018.

[30] S. Zhao, H. Fu, M. Gong, and D. Tao, “Geometry-aware symmetric domain adaptation for monocular depth estimation,” in *Proceedings of the IEEE/CVF conference on computer vision and pattern recognition*, pp. 9788–9798, 2019.

[31] J. N. Kundu, P. K. Uppala, A. Pahuja, and R. V. Babu, “Adadepth: unsupervised content congruent adaptation for depth estimation,” in *Proceedings of the IEEE conference on computer vision and pattern recognition*, pp. 2656–2665, 2018.

[32] C. Zheng, T.-J. Cham, and J. Cai, “T2net: synthetic-to-realistic translation for solving single-image depth estimation tasks,” in *Proceedings of the european conference on computer vision (ECCV)*, pp. 767–783, 2018.

[33] A. Bhoi, “Monocular depth estimation: a survey,” 2019.

[34] A. Dosovitskiy and T. Brox, “Generating images with perceptual similarity metrics based on deep networks,” *Advances in neural information processing systems*, vol. 29, pp. 658–666, 2016.

[35] J. Deng, W. Dong, R. Socher, L.-J. Li, K. Li, and L. Fei-Fei, “Imagenet: A large-scale hierarchical image database,” in *2009 IEEE conference on computer vision and pattern recognition*, pp. 248–255, Ieee, 2009.

[36] M. Heusel, H. Ramsauer, T. Unterthiner, B. Nessler, and S. Hochreiter, “Gans trained by a two time-scale update rule converge to a local nash equilibrium,” *Advances in neural information processing systems*, vol. 30, 2017.

[37] P. Babakhani and P. Zarei, “Automatic gamma correction based on average of brightness,” *Advances in computer science: an international journal*, vol. 4, no. 6, pp. 156–159, 2015.

[38] K. He, X. Zhang, S. Ren, and J. Sun, “Deep residual learning for image recognition,” in *Proceedings of the IEEE conference on computer vision and pattern recognition*, pp. 770–778, 2016.

[39] O. Ronneberger, P. Fischer, and T. Brox, “U-Net: Convolutional networks for biomedical image segmentation,” in *Medical image computing and computer-assisted intervention – MICCAI 2015*, (Cham), pp. 234–241, Springer International Publishing, 2015.

[40] C. Angermann, M. Haltmeier, R. Steiger, S. Pereverzyev, and E. Gizewski, “Projection-based 2.5D U-net architecture for fast volumetric segmentation,” in *2019 13th international conference on sampling theory and applications (SampTA)*, pp. 1–5, IEEE, 2019.

[41] N. Tajbakhsh, L. Jeyaseelan, Q. Li, J. N. Chiang, Z. Wu, and X. Ding, “Embracing imperfect datasets: A review of deep learning solutions for medical image segmentation,” *Medical Image Analysis*, vol. 63, p. 101693, 2020.

[42] M. Abadi, P. Barham, J. Chen, Z. Chen, A. Davis, J. Dean, M. Devin, S. Ghemawat, G. Irving, M. Isard, *et al.*, “Tensorflow: a system for large-scale machine learning,” in *12th USENIX symposium on operating systems design and implementation (OSDI 16)*, pp. 265–283, 2016.

[43] E. Wood, T. Baltrusaitis, C. Hewitt, S. Dziadzio, T. J. Cashman, and J. Shotton, “Fake it till you make it: face analysis in the wild using synthetic data alone,” in *Proceedings of the IEEE/CVF international conference on computer vision*, pp. 3681–3691, 2021.

[44] C.-H. Lee, Z. Liu, L. Wu, and P. Luo, “Maskgan: Towards diverse and interactive facial image manipulation,” in *Proceedings of the IEEE/CVF Conference on Computer Vision and Pattern Recognition*, pp. 5549–5558, 2020.

[45] S. Yang, P. Luo, C.-C. Loy, and X. Tang, “From facial parts responses to face detection: A deep learning approach,” in *2015 IEEE international conference on computer vision (ICCV)*, pp. 3676–3684, 2015.

A 3D Databases - An Overview

Single-shot depth estimation has become increasingly popular over the last decade of deep learning. The first deep learning solutions for depth synthesis were motivated by the development of autonomous driving and localization systems and therefore were initially designed to automatically determine the depth of indoor or outdoor scenes [14, 15, 16, 17, 29, 30, 31]. Deep convolutional neural networks, trained on large-scale and extensive data sets such as KITTI [2] or NYU Depth Dataset v2 [1] achieved state-of-the-art results. The outdoor video clips of the KITTI dataset can be used for various subtasks in computer vision such as optical flow, object detection, semantic segmentation and depth [3]. Each video sequence of the KITTI dataset consists of stereo image pairs with aligned depth images (LIDAR), which renders the database a common benchmark for unsupervised or self-supervised depth estimation tasks [16, 17, 29]. The NYU Depth Dataset v2 focuses on monocular sequences of indoor environments, where depth counterparts are obtained with a high quality RGB-D camera. Therefore, this dataset is considered a primary benchmark in supervised monocular depth estimation [14, 15].

With the advent of virtual and augmented reality applications, single-image pose estimation and 3D reconstruction of human bodies or body parts received a great amount of attention in the research field of computer vision [18]. 3D information on human faces provides additional benefits for face recognition or detection systems [6]. The Texas-3DFRD [12] and the Bosphorus-3DFA [11] are known representatives of paired face RGB-depth data of high quality and include a variety of head poses and emotional expressions. Both databases provide facial landmarks for additional face expression analysis, but with approximately 100 different individuals each, the sets are rather small. A larger number of facial depth models can be derived from 3D synthetic data of human faces as in [7, 43]. Leveraging the task to whole body depth estimation is challenging due to the fact that RGB-depth pairs of real individuals are not abundant in many datasets. A small dataset of 25 video clips for detailed human depth estimation is proposed in [10] while a depth dataset of 10 sequences recorded from different viewpoints is published in [8]. The Human3.6M dataset [13] contains high-resolution depth data from 11 individuals acting in varying scenarios. [9] propose using the approximately 68k video clips of synthetic humans in the large-scale SURREAL dataset for supervised training of human body depth and segmentation models.

B Network Details

In the following, **k** denotes the kernel size, **s** the stride, and **chns** the number of layer output channels. **Input** corresponds to the input of each layer. Network input and output are denoted by \mathcal{I} and \mathcal{O} , respectively, where for a generator network the output channel size equals 1 (RGB-to-depth) or 3 (depth-to-RGB).

Table 4: **DCGAN critic.** LReLU denotes the Leaky ReLU activation function with slope parameter 0.2. Global average pooling (global-avg) is used as pooling operation. Convolution layers followed by a layer normalization are denoted by conv-norm.

name	type	k	s	chns	input	activation
con1	conv-norm	4	2	64	\mathcal{I}	LReLU
con2	conv-norm	4	2	128	con1	LReLU
con3	conv-norm	4	2	256	con2	LReLU
con4	conv-norm	4	2	512	con3	LReLU
con5	conv-norm	4	1	512	con4	LReLU
con6	conv-norm	4	1	1024	con5	LReLU
pool	global-avg			1024	con6	
\mathcal{O}	dense			1	pool	linear

Table 5: **PatchGAN critic.** LReLU denotes the Leaky ReLU activation function with slope parameter 0.2. Convolution layers followed by a layer normalization are denoted by conv-norm.

name	type	k	s	chns	input	activation
con1	conv-norm	4	2	64	\mathcal{I}	LReLU
con2	conv-norm	4	2	128	con1	LReLU
con3	conv-norm	4	2	256	con2	LReLU
con4	conv-norm	4	2	512	con3	LReLU
con5	conv-norm	4	1	512	con4	LReLU
con6	conv-norm	4	1	1024	con5	LReLU
\mathcal{O}	convolution	4	1	1	con6	linear

Table 6: ResNet18 generator. The encoder is quite similar to the illustrated architecture in [38]. The decoder architecture is a slightly modified version of [17]. For upsampling, nearest neighbor method is used. Convolution layers followed by an instance normalization are denoted by conv-norm.

name	type	k	s	chns	input	activation
con1	conv-norm	7	2	64	\mathcal{I}	ReLU
max1	maxpool 3x3		2	64	con1	
res1	res-block	3	1	64	max1	ReLU
res2	res-block	3	1	64	res1	ReLU
res3	res-block	3	2	128	res2	ReLU
res4	res-block	3	1	128	res3	ReLU
res5	res-block	3	2	256	res4	ReLU
res6	res-block	3	1	256	res5	ReLU
res7	res-block	3	2	512	res6	ReLU
res8	res-block	3	1	512	res7	ReLU
ups1	upsampling		2	512	res8	
con2	conv-norm	3	1	512	ups1	ELU
cct1	concatenate			768	con2,res6	
con3	conv-norm	3	1	512	cct1	ELU
ups2	upsampling		2	512	con3	
con4	conv-norm	3	1	256	ups2	ELU
cct2	concatenate			384	con4,res4	
con5	conv-norm	3	1	256	cct2	ELU
ups3	upsampling		2	256	con5	
con6	conv-norm	3	1	128	ups3	ELU
cct3	concatenate			192	con6,res2	
con7	conv-norm	3	1	128	cct3	ELU
ups4	upsampling		2	128	con7	
con8	conv-norm	3	1	64	ups4	ELU
cct4	concatenate			128	con8,con1	
con9	conv-norm	3	1	64	cct4	ELU
ups5	upsampling		2	64	con9	
con10	conv-norm	3	1	32	ups5	ELU
con11	conv-norm	3	1	32	con10	ELU
\mathcal{O}	convolution	3	1	3/1	con11	tanh

Table 8: Residual block. A residual block (res-block) with kernel size k , stride s and channel size c is implemented as follows:

name	type	k	s	chns	input	activation
con1	conv-norm	k	s	c	\mathcal{I}	ReLU
con2	conv-norm	k	s	c	con1	
skip	conv-norm	1	s	c	\mathcal{I}	
add	addition			c	con2,skip	
\mathcal{O}	activation			c	add	ReLU

Table 7: U-net generator. The network design is motivated by [39]. For upsampling, transposed convolution (trans-conv) is used. Convolution layers followed by an instance normalization are denoted by conv-norm.

name	type	k	s	chns	input	activation
con11	conv-norm	3	1	48	\mathcal{I}	ReLU
con12	conv-norm	3	1	48	con11	ReLU
con13	conv-norm	3	2	48	con12	ReLU
con21	conv-norm	3	1	96	con13	ReLU
con22	conv-norm	3	1	96	con21	ReLU
con23	conv-norm	3	2	96	con22	ReLU
con31	conv-norm	3	1	192	con23	ReLU
con32	conv-norm	3	1	192	con31	ReLU
con33	conv-norm	3	2	192	con32	ReLU
con41	conv-norm	3	1	384	con33	ReLU
con42	conv-norm	3	1	384	con41	ReLU
con43	conv-norm	3	2	384	con42	ReLU
con51	conv-norm	3	1	768	con43	ReLU
con52	conv-norm	3	1	768	con51	ReLU
ups1	trans-conv	3	2	384	con52	ReLU
cct1	concatenate			768	ups1,con42	
con61	conv-norm	3	1	384	cct1	ReLU
con62	conv-norm	3	1	384	con61	ReLU
ups2	trans-conv	3	2	192	con62	ReLU
cct2	concatenate			384	ups2,con32	
con71	conv-norm	3	1	192	cct2	ReLU
con72	conv-norm	3	1	192	con71	ReLU
ups3	trans-conv	3	2	96	con72	ReLU
cct3	concatenate			192	up3,con22	
con81	conv-norm	3	1	96	cct3	ReLU
con82	conv-norm	3	1	96	con81	ReLU
ups4	trans-conv	3	2	48	con82	ReLU
cct4	concatenate			96	ups4,con12	
con91	conv-norm	3	1	48	cct4	ReLU
con92	conv-norm	3	1	48	con91	ReLU
\mathcal{O}	convolution	3	1	3/1	con92	tanh

C Facial Depth Estimation - Further Experiments

Section 4.2 demonstrates the plausibility of our proposed framework for fully unsupervised facial depth estimation using the small Texas-3DFRD [12]. Obviously, the shooting position of the portrayed faces is always constant. The data set consists exclusively of frontal views, the illumination direction is consistent and all images are individually cropped to the facial region. However, the goal of this section is to train a model that is capable of generating depth profiles from arbitrary portrait images that are at least sufficient for reasonable viewpoint augmentation. To accomplish this, we make use of the following two data sets: the Bosphorus Database for 3D Face Analysis (Bosphorus-3DFA) [11] and the CelebAMask-HQ [44] that records face portraits.

The Bosphorus-3DFA consists of 105 individuals, where for each person, in contrast to the Texas-3DFRD, varying poses, different head rotations and occlusions (e.g. eyeglasses, long hair) are available. Pixel-aligned depth samples represent absolute depth and are preprocessed to the range $[0, 1]$. Analogously to Section 4.2, we resize all RGB frames and depth profiles to a dimension of 256×256 and conduct data augmentation via random cropping. This results into 11k samples per modality. Although this database now contains different positions and face expressions, the decisive disadvantage is that all images were taken with constant lighting and with the same background (cf. Figure 9). Therefore, we add the CelebAMask-HQ to our experiment.

The CelebAMask-HQ is a large-scale facial portrait dataset with high-resolution face images of 30k celebrities selected from the CelebA dataset [45]. Each sample is provided with a segmentation mask of face attributes, and therefore this database is used to train and evaluate face analysis, face recognition and segmentation algorithms. In our opinion, this database is particularly well suited for depth prediction of arbitrary portraits, as it consists of RGB images with different exposures and different image backgrounds. Furthermore, all images are already cropped to a face-bounding box. We randomly select 10k RGB frames and resize them to a dimension of 256×256 .

The RGB images of the Bosphorus-3DFA and all samples of the CelebAMask-HQ are used as training data for the RGB domain, the depth profiles of the Bosphorus-3DFA are used for the depth domain. We consider now a semi-supervised approach, since we are given paired RGB and depth data in the Bosphorus-3DFA. To be more exact, we pretrain the RGB-to-depth generator G_{θ_y} in Algorithm 1 on the Bosphorus-3DFA in a supervised manner by minimizing the MAE between the depth predictions and the corresponding ground truths. After this step, we add the RGB samples of the CelebAMask-HQ to the input domain and continue with unsupervised training of our proposed framework as described in Algorithm 1. During optimization, RGB images are scaled from $[0, 255]$ to $[-1, 1]$ and depth profiles are scaled from $[0, 1]$ to $[-1, 1]$. We visually evaluate the success of the proposed semi-supervised approach and present in Figure 10 depth predictions and 3D models that were created from RGB images of the Bosphorus-3DFA, the CelebAMask-HQ, and members of our research group.



Figure 9: Left: RGB samples of the Bosphorus-3DFA [11]. Left: Samples of the CelebAMask-HQ [44].



Figure 10: From left to right: RGB input, depth profile estimated by our proposed framework (ResNet18 generator) and examples for viewpoint augmentation using the synthesized 3D face model.